ResearchGate

See discussions, stats, and author profiles for this publication at: https://www.researchgate.net/publication/23276166

Spectroscopic and Computational Studies of (μ-Oxo)(μ-1,2-peroxo)diiron(III) Complexes of Relevance to Nonheme Diiron Oxygenase Intermediates†

ARTICLE *in* THE JOURNAL OF PHYSICAL CHEMISTRY A · OCTOBER 2008

Impact Factor: 2.69 · DOI: 10.1021/jp8038225 · Source: PubMed

CITATIONS
18

READS
80

8 AUTHORS, INCLUDING:

Adam T Fiedler
Marquette University
36 PUBLICATIONS **778** CITATIONS

SEE PROFILE

József Kaizer
University of Pannonia, Veszprém
121 PUBLICATIONS **1,963** CITATIONS

SEE PROFILE

Stéphane Torelli
French National Centre for Scientific Research
27 PUBLICATIONS **1,027** CITATIONS

SEE PROFILE

Lawrence Que
University of Minnesota Twin Cities
451 PUBLICATIONS **25,894** CITATIONS

SEE PROFILE

Available from: József Kaizer
Retrieved on: 23 January 2016

NIH Public Access
Author Manuscript
J Phys Chem A. Author manuscript; available in PMC 2009 December 18.

Published in final edited form as:
J Phys Chem A. 2008 December 18; 112(50): 13037–13044. doi:10.1021/jp8038225.

Spectroscopic and Computational Studies of (μ-Oxo)(μ-1,2-peroxo)diiron(III) Complexes of Relevance to Nonheme Diiron Oxygenase Intermediates

Adam T. Fiedler[#], **Xiaopeng Shan**[#], **Mark P. Mehn**[#], **József Kaizer**[#], **Stéphane Torelli**[#], **Jonathan R. Frisch**[#], **Masahito Kodera**[‡], and **Lawrence Que Jr.**[#]

[#]Department of Chemistry and Center for Metals in Biocatalysis, 207 Pleasant St. S.E., University of Minnesota, Minneapolis, Minnesota 55455, U.S.A.

[‡]Department of Molecular Science and Technology, Doshisha University, Tatara Miyakotani 1-3, Kyotanabe 610-0321, JAPAN

Abstract

With the goal of gaining insight into the structures of peroxo intermediates observed for oxygen activating nonheme diiron enzymes, a series of metastable synthetic diiron(III)-peroxo complexes with $[Fe^{III}_2(\mu\text{-}O)(\mu\text{-}1,2\text{-}O_2)]$ cores has been characterized by X-ray absorption and resonance Raman spectroscopy. EXAFS analysis shows that this basic core structure gives rise to an Fe-Fe distance of ~3.15 Å; the distance is decreased by 0.1 Å upon introduction of an additional carboxylate bridge. In corresponding resonance Raman studies, vibrations arising from both the Fe-O-Fe and the Fe-O-O-Fe units can be observed. A change in the Fe-Fe distance affects the ν(O-O) mode, as well as the ν_{sym}(Fe-O-Fe) and the ν_{asym}(Fe-O-Fe) modes. Indeed a linear correlation can be discerned between the ν(O-O) frequency of a complex and its Fe-Fe distance among the subset of complexes with $[Fe^{III}_2(\mu\text{-}OR)(\mu\text{-}1,2\text{-}O_2)]$ cores (R = H, alkyl, aryl, or no substituent). These experimental studies are complemented by a normal coordinate analysis and DFT calculations.

Introduction

Nonheme diiron centers have been found in the active sites of a number of metalloenzymes involved in oxygen activation.[1,2] These enzymes have diverse and essential biological functions such as the hydroxylation of methane in methane monooxygenase (MMO) and of toluene in toluene 4-monooxygenase, the generation of the catalytically essential Tyr radical in Class I ribonucleotide reductases (RNR), and the desaturation of saturated fatty acids in fatty acid desaturases. In the course of oxygen activation, O_2 binds to the diiron(II) center to form a peroxodiiron(III) intermediate, which in turn undergoes O-O bond cleavage to form high-valent intermediates, such as the diiron(IV) intermediate **Q** of MMO[3–5] and the diiron(III,IV) intermediate **X** of RNR.[6,7] Of great interest is the nature of the diiron(III)-peroxo intermediates generated by these enzymes, which to date has not been established. These intermediates have been found to exhibit a range of ν(O-O) frequencies (898 cm^{-1} for stearoyl-acyl carrier protein Δ^9-desaturase,[8] 870 cm^{-1} for RNR W48F/D84E-R2,[9] and 851 cm^{-1} for frog ferritin[10]). Developing a rationale for the different frequencies would be helpful in deducing the structures of the corresponding intermediates.

Biomimetic complexes can contribute significantly to our understanding of such transient species. Indeed there are now five reported crystal structures of (μ-peroxo)diiron(III) complexes, all with 1,2-peroxo bridges.[11–14] In these structures, the Fe-O-O-Fe units are supported by additional bridging ligands such as oxo, hydroxo, alkoxo, and/or carboxylato bridges. This study focuses on complexes with the (μ-oxo)(μ-1,2-peroxo)diiron(III) core, some

NIH-PA Author Manuscript
NIH-PA Author Manuscript
NIH-PA Author Manuscript

NIH-PA Author Manuscript

NIH-PA Author Manuscript

NIH-PA Author Manuscript

of which have been reported to exhibit the lowest O-O frequencies among the diiron(III)-peroxo complexes thus far.[15–17] In this paper several complexes with the (μ-oxo)(μ-1,2-peroxo)diiron(III) core are investigated in detail by resonance Raman and X-ray absorption spectroscopies. Density-functional theory (DFT) calculations are used to aid in the interpretation of the spectroscopic data.

Experimental Section

Syntheses

Commercially available chemicals were purchased and used without further purification. The diiron(III) complexes, $[Fe^{III}_2(O)(OH)(BQPA)_2](OTf)_3$, $[Fe^{III}_2(O)(OH)(6\text{-}Me_3\text{-}TPA)_2](OTf)_3$ and $[Fe^{III}_2(O)(AcO)_2(BPPE)](ClO_4)_2$, were synthesized according to published methods[17–19] (see Scheme 1 for ligand structures). Elemental analyses were performed at Atlantic Microlab, Inc. (Norcross, GA). *Caution: Perchlorate salts are potentially explosive and should be handled with care!*

Bis(2-quinolylmethyl)-6-methylpyridyl-2-methylamine. (6-Me-BQPA)

To a solution of 2-cholromethylquinoline hydrochloride (3.5 g, 15.25 mmol) in MeCN (200 mL) at 0 °C was added Na_2CO_3 (9.6 g, 92 mmol); this mixture was then heated up to 82 °C and stirred for 30 min, 2-aminomethyl-6-methylpyridine (0.9 g, 7.62 mmol) was added and the resulting mixture was refluxed. After 3 days, the mixture was cooled to room temperature and filtered to remove solid. The filtrate was evaporated to dryness under vacuum, and the crude solid was recrystallized from hexane/ether (80/20) to obtain a pale yellow powder (85 %). ^{1}H NMR ($CDCl_3$): δ (ppm) 8.12 (d, 2H), 8.05 (d, 2H), 7.74 (m, 8H), 7.5 (m, 2H), 7.01 (d, 1H), 4.12 (s, 4H), 2.52 (s, 4H).

$[Fe^{III}_2(O)(OH)(6\text{-}Me\text{-}BQPA)_2](OTf)_3$

To a solution of bis(2-quinolylmethyl)-6-methylpyridyl-2-methylamine (0.405 g, 1 mmol) and $Fe(MeCN)_2(OTf)_2$ (0.436 g, 1 mmol) in dry MeCN (5 mL) at −40 °C was added *tert*-butyl hydroperoxide in nonane (0.22 mL, 1 mmol). After the color of the solution changed to dark red, this mixture was warmed up slowly to room temperature and 20 mL dry THF was layered above the solution. After two days, red crystals were deposited out in about 60% yield. Anal. Calcd for $[Fe^{III}_2(O)(OH)(6\text{-}Me\text{-}BQPA)_2](OTf)_3{\cdot}H_2O$ or $C_{57}H_{51}F_9Fe_2N_8O_{12}S_3$ (Found): C, 48.25 (48.00); H, 3.62 (3.75); F, 12.05 (12.09); N, 7.90 (7.72); S, 6.78 (6.58).

Preparation of $Fe^{III}_2(O)(O_2)$ intermediates

For the generation of intermediates **1, 2**, and **3**, a MeCN solution of the $Fe^{III}_2(\mu\text{-}O)(\mu\text{-}OH)(L)_2$ precursor was treated with 1 equiv triethylamine at −40 °C to generate the corresponding $Fe^{III}_2(\mu\text{-}O)_2$ complex. To this solution was added 10 equiv H_2O_2 to produce the $Fe^{III}_2(\mu\text{-}O)(\mu\text{-}1,2\text{-}O_2)(L)_2$ intermediate (**1**, L = 6-Me-BQPA; **2**, L = BQPA; **3**, L = 6-Me_3-TPA). Intermediate **4** was obtained by the reaction of its diiron(III) precursor $[Fe^{III}_2(O)(OAc)_2(BPPE)]^{2+}$ with 2 equiv triethylamine and 10 equiv H_2O_2 in MeCN at −40 °C. Conversions of diiron(III) precursors to corresponding peroxo intermediates were estimated to be >90% on the basis of extinction coefficients previously reported for **2**,[16] **3**,[15] and **4**.[17]

Physical methods

^{1}H NMR spectra were recorded on a Varian Unity 300 spectrometer at ambient temperature. Chemical shifts (in ppm) were referenced to the residual protonic solvent peaks. UV-vis spectra were recorded on a Hewlett-Packard 8453 diode array spectrophotometer. Resonance Raman spectra were collected on an ACTON AM-506M3 monochromator with a Princeton LN/CCD data collection system using Spectra-Physics models 2060 krypton ion and 2030-15 argon ion

NIH-PA Author Manuscript

NIH-PA Author Manuscript

NIH-PA Author Manuscript

lasers. Low-temperature spectra of peroxo intermediates in CH_3CN were obtained at 77 K using a 135° backscattering geometry. Samples were frozen onto a gold-plated copper cold finger in thermal contact with a dewar containing liquid nitrogen. Raman frequencies were referenced to the features of indene. Slits were set for a band-pass of 4 cm^{-1} for all spectra.

XAS data collection

XAS data were collected on beamline X9B at the National Synchrotron Light Source (NSLS) of Brookhaven National Laboratory (BNL). Fe K-edge X-ray absorption spectra were recorded on frozen solutions at around 16 K over the energy range 6.9–8.0 keV as previously described.[20–22] The storage ring condition was: 2.8 GeV, 100–300 mA. The beam vertical aperture of the pre-monochromator slits was 1 mm. Contamination of higher harmonics radiation was minimized by utilizing a harmonic rejection. The horizontal spot size of the beam on the sample was 4–6 mm. Spectra were measured with 10 eV steps below the edge, 0.3 eV steps in the edge region, and steps equivalent to 0.05 $Å^{-1}$ increments above the edge (region borders were 6932, 7102, and 7137 eV). An iron foil spectrum was concomitantly recorded for internal energy calibration, and the first inflection point of the K-edge energy was calibrated to 7112.0 eV. The data were recorded in fluorescence excitation mode ($A_{exp} = (C_f/C_0)$) using a solid state 13 element Ge detector.

Data analysis

Standard procedures were used to analyze the XAS data. The pre-edge background intensity was eliminated by fitting a Gaussian function to the background and a three-segment spline with fourth-order polynomial components was used to remove low-frequency background.[23] The resulting spectra were then treated with *SSExafs*[20,24] in order to obtain near-edge XAS (XANES) parameters. The edge was modeled as an integral of a 75% Gaussian and a 25% Lorentzian peak and the heights, positions, and widths (at half height) of the Gaussian pre-edge peaks were refined to fit the data. Pre-edge peak areas are reported as percentage of the Fe K-edge height × eV and multiplied by 100.

Analysis of the EXAFS data was performed using the program *EXAFSPAK*.[25] EXAFS refinement was carried out on $k^3\chi(k)$ data, using the phase and amplitude functions obtained from *FEFF*.[26] EXAFS data fittings were performed using the back-transformation ranges provided in Table 2. For each fit, the parameters r and σ^2 were optimized, while n was kept fixed. n was then systematically varied in integer steps. The goodness of fit (GOF) was determined using the formula: $GOF = \Sigma\,(\chi_{calc} - \chi_{exp})^2 / N$, where N is the number of data points. The threshold energy (E_0) was also varied, although it was maintained at a common value for all shells.

DFT Calculations

Geometry optimizations of $[Fe^{III}_2(\mu\text{-}O)(\mu\text{-}1,2\text{-}O_2)(6\text{-}Me_3\text{-}TPA)_2]^{2+}$ were performed with the Amsterdam Density Functional (ADF) 2004.01 software package[27–29] on a cluster of 10 processors (Ace computers) using ADF basis set IV (triple-ζ with single polarization on the ligand atoms), an integration constant of 4.0, and the Vosko-Wilk-Nusair local density approximation[30] with the nonlocal gradient corrections of Becke[31] and Perdew.[32] Antiferromagnetic coupling between the two Fe(III) centers was incorporated into the DFT calculations with the construction of broken-symmetry (BS) wavefunctions,[33–35] in which the spin-up (α) and spin-down (β) electrons were localized on Fe1 and Fe2, respectively. Although the BS state is not a pure spin state (its wavefunction is an eigenfunction of M_s, not S^2), Noodleman and coworkers have demonstrated that this approach reasonably approximates the antiferromagnetic ground state and provides accurate geometries.[36] The Cartesian coordinates for the DFT geometry-optimized model are available in the Supporting Information (Table S1).

NIH-PA Author Manuscript

NIH-PA Author Manuscript

NIH-PA Author Manuscript

Normal Coordinate Analysis (NCA)

Normal coordinate calculations used a general valence force field,[37] and were performed using the QCPE program 576 developed by Peterson and McIntosh, which solves the vibrational secular equation **GFL** = λ**L**.[38] For complex **1**, the large size of the molecule forced us to use a smaller model that included only the [Fe_2O_3] core. Structural parameters were derived from DFT geometry optimizations. Given the idealized C_{2v} symmetry of the [Fe_2O_3] unit, only one force constant was used to describe the Fe-O_{oxo} and Fe-O_{peroxo} stretching motions. Additionally, a small Fe···Fe force constant of +0.50 mdyn/Å was included to model the nonbonded interaction between the two Fe atoms (essentially, this mode accounts for the symmetric O-Fe-O and Fe-O-Fe bending motions). Five interaction force constants were included to account for kinematic coupling between the stretching motions of the Fe-O_{oxo}/Fe-O_{peroxo}/O-O bonds, as well as between the these motions and the Fe···Fe stretch. These parameters were then optimized to fit the experimentally determined frequencies, although the *F*(Fe···Fe) value was fixed. The resulting force constants are summarized in the Supporting Information (Table S3).

Results and Discussion

Four metastable Fe^{III}_2(μ-O)(μ-1,2-O_2) complexes were generated at low temperature from the reaction of diiron(III) precursors with H_2O_2, as depicted in Scheme 2. Intermediates **1–3** have supporting tetradentate tripodal ligands, while **4** is supported by a hexadentate dinucleating ligand that provides only three ligands in a facial array per iron (Scheme 1). Thus intermediate **4** differs from the other three in having an additional carboxylate bridge that completes the distorted octahedral coordination sphere about each iron. These complexes exhibit two intense visible absorption features with maxima near 500 and 650 nm; there is also a much weaker near IR band near 800 nm for **1–3** (Figure 1). These intermediates are further characterized by X-ray absorption and resonance Raman spectroscopies in this study, and detailed analyses are presented below.

1. XAS studies of Fe^{III}_2(O)(O_2) intermediates

As the low thermal stability of the Fe_2(O)(O_2) intermediates made X-ray crystallography unfeasible as a method for obtaining structural information, X-ray absorption spectroscopy (XAS) was adopted as an alternative method for structural characterization of these short-lived species. X-ray absorption spectra at the Fe K-edge were measured for three Fe_2(O)(O_2) species **1, 2** and **4** (complex **3** was studied previously[15]) and the resulting XANES and EXAFS data are presented in Figure 2 and Figure 3, respectively. Figure 2 compares the near-edge regions of the three complexes, which provides information regarding the oxidation states and coordination environments of the metal centers. The first inflection point of the rising edge was assigned as the edge energy (E_0) associated with the transition of an electron from the Fe 1s orbital to the continuum. The values for **1, 2**, and **4** are typical of iron(III) centers (Table 1). The energy of the pre-edge feature ($E_{preedge}$), at about 8–10 eV below the edge jump, corresponds to the Fe 1s→3d transitions. Interestingly, the pre-edge transition for **4** is more intense than those for **1** and **2**, indicative of a larger deviation from a centrosymmetric geometry in the case of **4**.

The filtered Fe K-edge EXAFS data for complexes **1**, **2** and **4**, along with the corresponding Fourier transforms (FT, *R′* space), are shown in Figure 3 (the unfiltered data are shown in Figure S1). All three Fe_2(O)(O_2) species exhibit first-shell features between *r*’ = ~1.0 and 2.2 Å and one or more prominent second-shell peaks between *r*’ = 2.5 and 3.1 Å (where *r*’ is the actual metal-scatterer distance after a phase-shift correction of approximately 0.4 Å). Our EXAFS analysis of **1** revealed that the first coordination sphere consists of two O/N atoms at 1.83 Å, three N/O atoms at 2.23 Å, and an intermediate N/O scatterer at 2.05 Å (Table 2). The

NIH-PA Author Manuscript

NIH-PA Author Manuscript

NIH-PA Author Manuscript

intense second-shell feature at *r*' = ~ 2.85 Å is well fit by a single Fe scatterer at 3.15 Å, thus providing strong evidence that **1** is indeed a dinuclear complex. Proper fitting of the data also required an additional shell of 4–6 C atoms near 3.0 Å, consistent with several earlier EXAFS studies of Fe complexes with TPA-type ligands.[22,39,40]

Given the similarity of their supporting ligands, it is not surprising that the bond distances obtained by EXAFS for **2** are nearly identical those found for **1** (Table 2). Importantly, the bond distances derived for **1** and **2** are quite similar to those found previously for the closely related complex, $[Fe^{III}_2(O)(O_2)(6\text{-}Me_3\text{-}TPA)_2]^{2+}$ (**3**) (Table 2).[15] Thus, despite minor differences, we can conclude that complexes **1–3** generally share the same Fe coordination environments. The two short Fe-ligand bonds at ~1.8 Å are then assigned to the bridging oxo and peroxo groups, while the four remaining first-sphere atoms between 2.02 and 2.23 Å are supplied by the N_4 supporting ligands.

These results are further supported by DFT computations performed on $[Fe_2(O)(O_2)(6\text{-}Me_3\text{-}TPA)_2]^{2+}$. These calculations assumed antiferromagnetically coupled high-spin Fe(III) centers and a μ-1,2 binding mode for the peroxo ligand. The resulting $Fe_2(O)(O_2)$ unit is nearly planar, with an average dihedral angle of 2.2°. As shown in Figure 4, the optimized model features Fe-O_{oxo} and Fe-O_{peroxo} bonds with nearly equal lengths of ~1.8 Å, in good agreement with the EXAFS-derived values of 1.81–1.84 Å. Moreover, the calculations point to considerable variation in the Fe-N bond distances, which is also reflected in the experimental fits. Finally, the computed Fe-Fe distance of 3.17 Å approaches the values of 3.13–3.15 Å found experimentally. Thus, our combined EXAFS/DFT approach confirms the formulation of complexes **1–3** as $[Fe^{III}_2(\mu\text{-}O)(\mu\text{-}1,2\text{-}O_2)(L)_2]^{2+}$.

Our EXAFS analysis of **4** shows that this complex deviates somewhat from the pattern established by **1–3**. For instance, it is not necessary to include a carbon shell at ~3 Å, which is often required for complexes of tetradentate TPA-like ligands. Moreover, fits 8–10 in Table 2, which vary with respect to the number of scatterers in each shell of the first coordination sphere, are equally good, although we favor fit 9 because it corresponds to shells with the most reasonable set of Debye-Waller (σ^2) values. The scatterer at 1.77 Å likely corresponds to the bridging oxo group, while the value of 1.94 Å represents the average of the Fe-O_{peroxo} and Fe-$O_{acetate}$ bond distances. Importantly, the data require an Fe scatterer at 3.04 Å (Table 2). This Fe-Fe distance is approximately 0.1 Å shorter than the values found for **1–3**, likely reflecting the presence of the additional carboxylate ligand bridging the Fe(III) centers.[41]

2. Resonance Raman studies of $Fe^{III}_2(O)(O_2)$ intermediates

Resonance Raman spectroscopy is a very useful tool for probing the vibrations of the $Fe_2(\mu\text{-}O)(\mu\text{-}1,2\text{-}O_2)$ core. In this study of **1–4**, vibrations are observed that can be associated with both the Fe-O-Fe and Fe-O-O-Fe substructures. For **1–3**, all five possible stretching vibrational modes of the Fe_2O_3 core have been observed and identified by isotope labeling and excitation profile experiments. The spectra are presented in Figure 5 and Figure 6, with spectra of complexes with Fe-^{16}O-Fe cores shown in black and those with Fe-^{18}O-Fe cores provided in red. The vibrational frequencies are tabulated in Table 3.

The vibrations of the Fe-O-O-Fe unit have been reported previously and consist of three modes: the O-O stretch and symmetric and asymmetric ν(Fe-O_2-Fe) deformations. Figure 5 shows the resonance Raman spectra of **1, 2**, and **3** obtained with 647.1 nm excitation, in resonance with the lower energy charge transfer (CT) transition. The O-O stretch is easily identified in the 850 cm^{-1} region, with an $^{16}O_2 \rightarrow {}^{18}O_2$ shift of 46 cm^{-1} that is consistent with a Hooke's Law calculation for a diatomic O-O unit. The ν_{sym}(Fe-O_2-Fe) mode is readily found below 500 cm^{-1} and exhibits an $^{16}O_2 \rightarrow {}^{18}O_2$ shift of 15–21 cm^{-1}. On the other hand, the ν_{asym}(Fe-O_2-Fe) mode is found above 500 cm^{-1} among vibrations of the Fe-O-Fe unit. In the case of **4**, only

NIH-PA Author Manuscript

NIH-PA Author Manuscript

NIH-PA Author Manuscript

the ν(O-O) mode is observed and is found at 830 cm^{-1}, which is about 20 cm^{-1} lower in energy than those of **1** – **3**.[45]

In contrast to modes involving the peroxo group, vibrations arising from the Fe-O-Fe unit of Fe^{III}_2(μ-O)(μ-1,2-O_2) complexes have not been previously noted. However, we readily observed such modes by shifting the laser excitation to higher energies, as shown in Figure 6. The modes were definitively assigned by incorporating ^{18}O into the oxo bridge. For **4**, only one vibration at 537 cm^{-1} is observed, which is assigned to the symmetric mode of the Fe-O-Fe unit. On the other hand, for **1** – **3**, both ν_{sym}(Fe-O-Fe) and ν_{asym}(Fe-O-Fe) modes can be identified. The symmetric modes are found near 500 cm^{-1} with $^{16}O \rightarrow {}^{18}O$ downshifts of 12–16 cm^{-1}, while the asymmetric modes are found near 700 cm^{-1} with $^{16}O \rightarrow {}^{18}O$ downshifts of 30–32 cm^{-1} (Table 3, Figure 6). The difference between **4** and the other three peroxo complexes can be ascribed to the symmetry of the Fe-O-Fe unit (Scheme 1). In **4**, the two individual Fe sites are identical, while those in **1** – **3** are distinct because the oxo bridge is *trans* to an amine on one Fe and *trans* to a pyridine on the other Fe. Indeed, our DFT computations of **3** confirm the asymmetry in the Fe-O_{oxo} bond lengths (Figure 4). Sanders-Loehr and coworkers have previously noted that the ν_{asym}(Fe-O-Fe) mode becomes observable in the resonance Raman spectrum of an Fe-O-Fe complex and increases in intensity as the Fe-O-Fe unit becomes more asymmetric.[46–48] This correlation rationalizes the spectral differences observed for **1** – **4**.

Previously, the ν_{sym}(Fe-O-Fe) and ν_{asym}(Fe-O-Fe) frequencies of (μ-oxo)diiron(III) complexes have been found to reflect the Fe-O-Fe angle.[18,49] When the values for **1–4** are interpreted within this framework, the Fe-O-Fe angles are deduced to be 120° for **1–3** and 110° for **4**, consistent with the differences in Fe-Fe distances determined by EXAFS analysis. Moreover, the predicted Fe-O-Fe angles for **1–3** agree nicely with the value of 121° computed by DFT for **3** (Figure 4).

The excitation profiles for the symmetric Fe-O-Fe and O-O stretching modes of complex **3** (peaks at 511 and 847 cm^{-1}, respectively) are shown in Figure 7. The corresponding profiles for **1, 2** and **4** are quite similar (Figure S3). The ν(O-O) mode is strongly enhanced by excitation into the broad absorption feature at 650 nm, confirming the assignment of this band as a peroxo■ Fe(III) charge transfer transition. Conversely, the peak corresponding to the symmetric ν(Fe-O-Fe) mode is enhanced at much shorter wavelengths, indicating that the intense peaks in the near-UV region have significant contributions from oxo■ Fe(III) CT transitions. Thus, our resonance Raman data provide considerable insights into the nature of the UV-vis absorption features.

An unexpected feature of our resonance Raman study is the slight sensitivity of the ca. 700 cm^{-1} mode associated with the Fe-O-Fe unit in **1–3** to ^{18}O-labeling of the peroxo ligand (Figure 5, Table 3). The $^{16}O_2 \rightarrow {}^{18}O_2$ downshift of 4 cm^{-1} in the case of **1** was also observed for the fully labeled $Fe_2(O)(O_2)$ core generated by using both $H_2{}^{18}O$ and $H_2{}^{18}O_2$. These observations suggest coupling between modes of the Fe-O-Fe and the Fe-O-O-Fe units. To further probe the vibrational dynamics of the $Fe_2(O)(O_2)$ core, we performed a normal coordinate analysis (NCA) using the resonance Raman data presented above. In fact, complexes **1–3** provide ideal systems for NCA due to the abundance of isotope-shift data available for all five stretching modes of the $Fe_2(O)(O_2)$ core (Table 3). The normal coordinate analyses described herein utilized a 5-atom model of the $Fe_2(O)(O_2)$ core derived from our DFT calculations (*vide supra*), in which the structural coordinates were symmetrized so as to obtain a molecule with strict C_{2v} symmetry (for more details see Experimental Section and Table S2). We limited our analysis to **1**, since vibrational data for the fully-labeled $Fe_2(^{18}O)(^{18}O_2)$ species were only available for this complex.

NIH-PA Author Manuscript

NIH-PA Author Manuscript

NIH-PA Author Manuscript

Table 4 compares the NCA-calculated and experimental frequencies for complex **1**. It is evident that the computed force field adequately reproduces both the vibrational frequencies and $^{16}O \rightarrow ^{18}O$ isotope hifts, with an average deviation of 2.2 cm^{-1}. The potential energy distributions (PEDs) reveal a small but significant degree of echanical coupling between the (Fe-O-Fe) and (Fe-O_2-Fe) stretching motions, with an average of ~7 % ν(Fe-O-Fe) character in the ν(Fe-O_2-Fe) modes, and vice versa. This accounts for the fact, noted above, that the peaks near 700 cm^{-1} associated with the Fe-O-Fe unit shift to lower frequencies upon ^{18}O-labeling of the peroxo ligand in **1–3**.

Relevant force constants derived from the NCA of **1** are shown in Table 5, along with the corresponding values obtained by Zhang *et al*. for [Fe_2(μ-O)(μ-1,2-O_2)(6-Me_2BPP)] (**B**) (where 6-Me_2-BPP is the same as 6-Me_3-TPA except that one of the pyridine rings has been replaced by a CH_2CO_2 moiety).[14] Although the peroxo O-O bonds have similar strengths in the two complexes, the Fe-O force constants are ~ 15 % larger for **1** than **B** (Table 5), suggesting that the anionic carboxylate group weakens the Fe-O bonds relative to neutral pyridine-type donors. A similar carboxylate ligand effect has been noted for the peroxo intermediate of RNR W48F/D84E R2.[50]

Summary and Perspectives

Our studies of the diiron(III)-peroxo complexes described above have provided insight into the structural and spectroscopic properties of the [Fe^{III}_2(μ-O)(μ-1,2-O_2)] core. When viewed from a broader perspective (Table 3), it is clear that the nature of the bridging ligands that support the Fe-O-O-Fe unit modulate the Fe-Fe distances and, in turn, the ν(O-O) frequencies. The Fe-Fe distance can be as large as 4 Å, as in the case of [$Fe_2(O_2)(Tp^{iPr2})_2(O_2CCH_2Ph)_2$] (**E**) where the (μ-1,2-peroxo)diiron(III) unit is supported by two bidentate carboxylate bridges. But the introduction of an oxo bridge dramatically decreases the Fe-Fe distance to ~3.15 Å, as found for **1** – **3**. Adding a carboxylate bridge as in **4** further shortens the Fe-Fe distance by 0.1 Å, while protonating or alkylating the oxo bridge lengthens the Fe-Fe distance to an intermediate value of ~3.4 Å (e.g. complexes **A, C**, and **D** in Table 3). These differences in Fe-Fe distance give rise to ν(O-O) frequencies that span a range of ~80 cm^{-1}. Indeed, as shown in Figure 8, ν(O-O) decreases with Fe-Fe distance for the major subset of complexes that form a five-membered [Fe^{III}_2(μ-OR)(μ-1,2-O_2)] ring (R = H, alkyl, aryl, or no substituent). This data set validates the mechanical coupling model for the [Fe^{III}_2(μ-1,2-O_2)] unit conceived by Brunold and Solomon.[44] However [$Fe_2(O_2)(Tp^{iPr2})_2(O_2CR)_2$] (**E**) does not belong to this subset and is a significant outlier. Unlike for those in the [Fe^{III}_2(μ-OR)(μ-1,2-O_2)] subset, the Fe-O-O-Fe dihedral angle for this complex is not constrained to be close to 0° and is in fact significantly larger than 0°, which may be why this complex does not fit with the correlation in Figure 8.

As noted in the introduction, the ν(O-O) frequencies of diiron(III)-peroxo intermediates in nonheme diiron enzymes exhibit wide variations despite close similarities in active site structures. Within this class, the peroxo intermediate of ferritin exhibits the lowest ν(O-O) frequency (851 cm^{-1}).[10] The presence of only one carboxylate bridge in the ferritin active site,[51] compared to two in RNR and Δ^9 desaturase,[52,53] allows space to incorporate solvent-derived monoatomic bridge(s) (like O^{2-} or HO^-). Thus, the peroxo intermediate of ferritin likely possesses a five-membered [Fe^{III}_2(μ-O(H))(μ-1,2-O_2)] ring, similar to those found in the model complexes studied herein. An EXAFS study of the ferritin peroxo intermediate reported a remarkably short Fe-Fe distance of 2.53 Å, leading to the proposal that the diferric center is bridged by two monoatomic ligands in addition to peroxide.[54] However, based on Figure 8, we would predict an Fe-Fe distance in the range of 3.1 to 3.2 Å, which is more consistent with a [Fe^{III}_2(μ-O)(μ-1,2-O_2)(μ-1,3-O_2CR)] structure. Of course, as with [$Fe_2(O_2)(Tp^{iPr2})_2(O_2CCH_2Ph)_2$] (**E**), the Fe-O-O-Fe unit in ferritin might adopt a non-planar geometry,

NIH-PA Author Manuscript

NIH-PA Author Manuscript

NIH-PA Author Manuscript

in which case the close connection between Fe-Fe distances and ν(O-O) frequencies may break down. Regardless, our results will likely prove useful for interpreting trends in ν(O-O) frequencies among diiron(III)-peroxo intermediates of nonheme diiron enzymes.

Supplementary Material

Refer to Web version on PubMed Central for supplementary material.

Acknowledgment

This research was supported by the US National Institutes of Health (grant GM-38767 to L.Q. and postdoctoral fellowship GM-079839 to A.T.F.). XAS data were collected on beamline X9B at the National Synchrotron Light Source (NSLS). NSLS is supported by the U.S. Department of Energy, Office of Science, Office of Basic Energy Sciences, under Contract No. DE-AC02-98CH10886. We thank Professor Thomas Brunold of the University of Wisconsin-Madison for graciously providing access to his computer cluster.

References and Notes

1. Wallar BJ, Lipscomb JD. Chem. Rev 1996;96:2625–2658. [PubMed: 11848839]
2. Merkx M, Kopp DA, Sazinsky MH, Blazyk JL, Müller J, Lippard SJ. Angew. Chem. Int. Ed 2001;40:2782–2807.
3. Lee S-K, Fox BG, Froland WA, Lipscomb JD, Münck E. J. Am. Chem. Soc 1993;115:6450–6451.
4. Liu KE, Valentine AM, Wang D, Huynh BH, Edmondson DE, Salifoglou A, Lippard SJ. J. Am. Chem. Soc 1995;117:10174–10185.
5. Shu L, Nesheim JC, Kauffmann K, Münck E, Lipscomb JD, Que L Jr. Science 1997;275:515–518. [PubMed: 8999792]
6. Sturgeon BE, Burdi D, Chen S, Huynh B-H, Edmondson DE, Stubbe J, Hoffman BM. J. Am. Chem. Soc 1996;118:7551–7557.
7. Riggs-Gelasco PJ, Shu L, Chen S, Burdi D, Huynh BH, Que L Jr, Stubbe J. J. Am. Chem. Soc 1998;120:849–860.
8. Broadwater JA, Ai J, Loehr TM, Sanders-Loehr J, Fox BG. Biochemistry 1998;37:14664–14671. [PubMed: 9778341]
9. Moënne-Loccoz P, Baldwin J, Ley BA, Loehr TM, Bollinger JM Jr. Biochemistry 1998;37:14659–14663. [PubMed: 9778340]
10. Moënne-Loccoz P, Krebs C, Herlihy K, Edmondson DE, Theil EC, Huynh BH, Loehr TM. Biochemistry 1999;38:5290–5295. [PubMed: 10220314]
11. Ookubo T, Sugimoto H, Nagayama T, Masuda H, Sato T, Tanaka K, Maeda Y, Okawa H, Hayashi Y, Uehara A, Suzuki M. J. Am. Chem. Soc 1996;118:701–702.
12. Dong Y, Yan S, Young VG Jr, Que L Jr. Angew. Chem. Int. Ed. Engl 1996;35:618–620.
13. Kim K, Lippard SJ. J. Am. Chem. Soc 1996;118:4914–4915.
14. Zhang X, Furutachi H, Fujinami S, Nagatomo S, Maeda Y, Watanabe Y, Kitagawa T, Suzuki M. J. Am. Chem. Soc 2005;127:826–827. [PubMed: 15656607]
15. Dong Y, Zang Y, Shu L, Wilkinson EC, Que L Jr, Kauffmann K, Münck E. J. Am. Chem. Soc 1997;119:12683–12684.
16. Kryatov SV, Taktak S, Korendovych IV, Rybak-Akimova EV, Kaizer J, Torelli S, Shan X, Mandal S, MacMurdo V, Mairata i Payeras A, Que L Jr. Inorg. Chem 2005;44:85–99. [PubMed: 15627364]
17. Kodera M, Taniike Y, Itoh M, Tanahashi Y, Shimakoshi H, Kano K, Hirota S, Iijima S, Ohba M, Okawa H. Inorg. Chem 2001;40:4821–4822. [PubMed: 11531426]
18. Zheng H, Zang Y, Dong Y, Young VG Jr, Que L Jr. J. Am. Chem. Soc 1999;121:2226–2235.
19. Zang Y, Pan G, Que L Jr, Fox BG, Münck E. J. Am. Chem. Soc 1994;116:3653–3654.
20. Scarrow RC, Maroney MJ, Palmer SM, Que L Jr, Roe AL, Salowe SP, Stubbe J. J. Am. Chem. Soc 1987;109:7857–7864.
21. Shu L, Chiou Y-M, Orville AM, Miller MA, Lipscomb JD, Que L Jr. Biochemistry 1995;34:6649–6659. [PubMed: 7756296]

NIH-PA Author Manuscript NIH-PA Author Manuscript NIH-PA Author Manuscript

22. Rohde J-U, Torelli S, Shan X, Lim MH, Klinker EJ, Kaizer J, Chen K, Nam W, Que L Jr. J. Am. Chem. Soc 2004;126:16750–16761. [PubMed: 15612713]
23. Klinker EJ, Jackson TA, Jensen MP, Stubna A, Juhász G, Bominaar EL, Münck E, Que L Jr. Angew. Chem. Int. Ed 2006;45:7394–7397.
24. Scarrow RC, Trimitsis MG, Buck CP, Grove GN, Cowling RA, Nelson MJ. Biochemistry 1994;33:15023–15035. [PubMed: 7999760]
25. George, GN.; Pickering, IJ. Stanford Synchrotron Radiation Laboratory. Stanford, California: Stanford Linear Accelerator Center; 2000.
26. Rehr JJ, Mustre de Leon J, Zabinsky SI, Albers RC. J. Am. Chem. Soc 1991;113:5135–5140.
27. te Velde G, Baerends EJ. J. Comput. Phys 1992;99:84–98.
28. Guerra CF, Snijders JG, te Velde G, Baerends EJ. Theor. Chem. Acc 1998;99:391–403.
29. ADF2003.01; SCM, Theoretical Chemistry. Amsterdam, The Netherlands: Vrije Universiteit; http://www.scm.com
30. Vosko SH, Wilk L, Nusair M. Can. J. Phys 1980;58:1200.
31. Becke AD. J. Chem. Phys 1986;84:4524–4529.
32. Perdew JP. Phys. Rev. B 1986;33:8822–8824.
33. Noodleman L, Case DA. Adv. Inorg. Chem 1992;38423-+
34. Noodleman L, Lovell T, Liu TQ, Himo F, Torres RA. Curr. Opin. Chem. Biol 2002;6:259–273. [PubMed: 12039013]
35. Noodleman L, Peng CY, Case DA, Mouesca JM. Coord. Chem. Rev 1995;144:199–244.
36. Torres RA, Lovell T, Noodleman L, Case DA. Journal of the American Chemical Society 2003;125:1923–1936. [PubMed: 12580620]
37. Wilson, EB.; Decius, JC.; Cross, PC. Molecular Vibrations; The Theory of Infrared and Raman Vibration Spectra. London: McGraw-Hill; 1955.
38. McIntosh DF, Peterson MR. 1989
39. Jensen MP, Costas M, Ho RYN, Kaizer J, Mairata i Payeras A, Münck E, Que L Jr, Rohde J-U, Stubna A. J. Am. Chem. Soc 2005;127:10512–10525. [PubMed: 16045338]
40. Rohde J-U, Stubna A, Bominaar EL, Münck E, Nam W, Que L Jr. Inorg. Chem 2006;45:6435–6445. [PubMed: 16878956]
41. A detailed EXAFS analysis was also performed on the unfiltered data of **4**. As shown in Table S2, the resulting structural parameters are almost identical to those obtained with the filtered data.
42. Dong Y, Ménage S, Brennan BA, Elgren TE, Jang HG, Pearce LL, Que L Jr. J. Am. Chem. Soc 1993;115:1851–1859.
43. Murch BP, Bradley FC, Que L Jr. J. Am. Chem. Soc 1986;108:5027–5028.
44. Brunold TC, Tamura N, Kitajima M, Moro-oka Y, Solomon EI. J. Am. Chem. Soc 1998;120:5674–5690.
45. The ν(O-O) of **4** was originally reported to be at 816 cm^{-1} in ref. #17, but a higher value was found in our experiments.
46. Gómez-Romero P, Witten EH, Reiff WM, Backes G, Sanders-Loehr J, Jameson GB. J. Am. Chem. Soc 1989:9039–9047.
47. Norman RE, Yan S, Que L Jr, Sanders-Loehr J, Backes G, Ling J, Zhang JH, O'Connor CJ. J. Am. Chem. Soc 1990;112:1554–1562.
48. Cohen JD, Payne S, Hagen KS, Sanders-Loehr J. J. Am. Chem. Soc 1997;119:2960–2961.
49. Sanders-Loehr J, Wheeler WD, Shiemke AK, Averill BA, Loehr TM. J. Am. Chem. Soc 1989;111:8084–8093.
50. Skulan AJ, Brunold TC, Baldwin J, Saleh L, Bollinger JM Jr, Solomon EI. J. Am. Chem. Soc 2004;126:8842–8855. [PubMed: 15250738]
51. Ha Y, Shi DS, Small GW, Theil EC, Allewell NM. J. Biol. Inorg. Chem 1999;4:243–256. [PubMed: 10439069]
52. Logan DT, Su X-D, Åberg A, Regnström K, Hajdu J, Eklund H, Nordlund P. Structure 1996;4:1053–1064. [PubMed: 8805591]
53. Lindqvist Y, Huang W, Schneider G, Shanklin J. EMBO J 1996;15:4081–4092. [PubMed: 8861937]

54. Hwang J, Krebs C, Huynh BH, Edmondson DE, Theil EC, Penner-Hahn JE. Science 2000;287:122–125. [PubMed: 10615044]

NIH-PA Author Manuscript

NIH-PA Author Manuscript

NIH-PA Author Manuscript

NIH-PA Author Manuscript

NIH-PA Author Manuscript

NIH-PA Author Manuscript

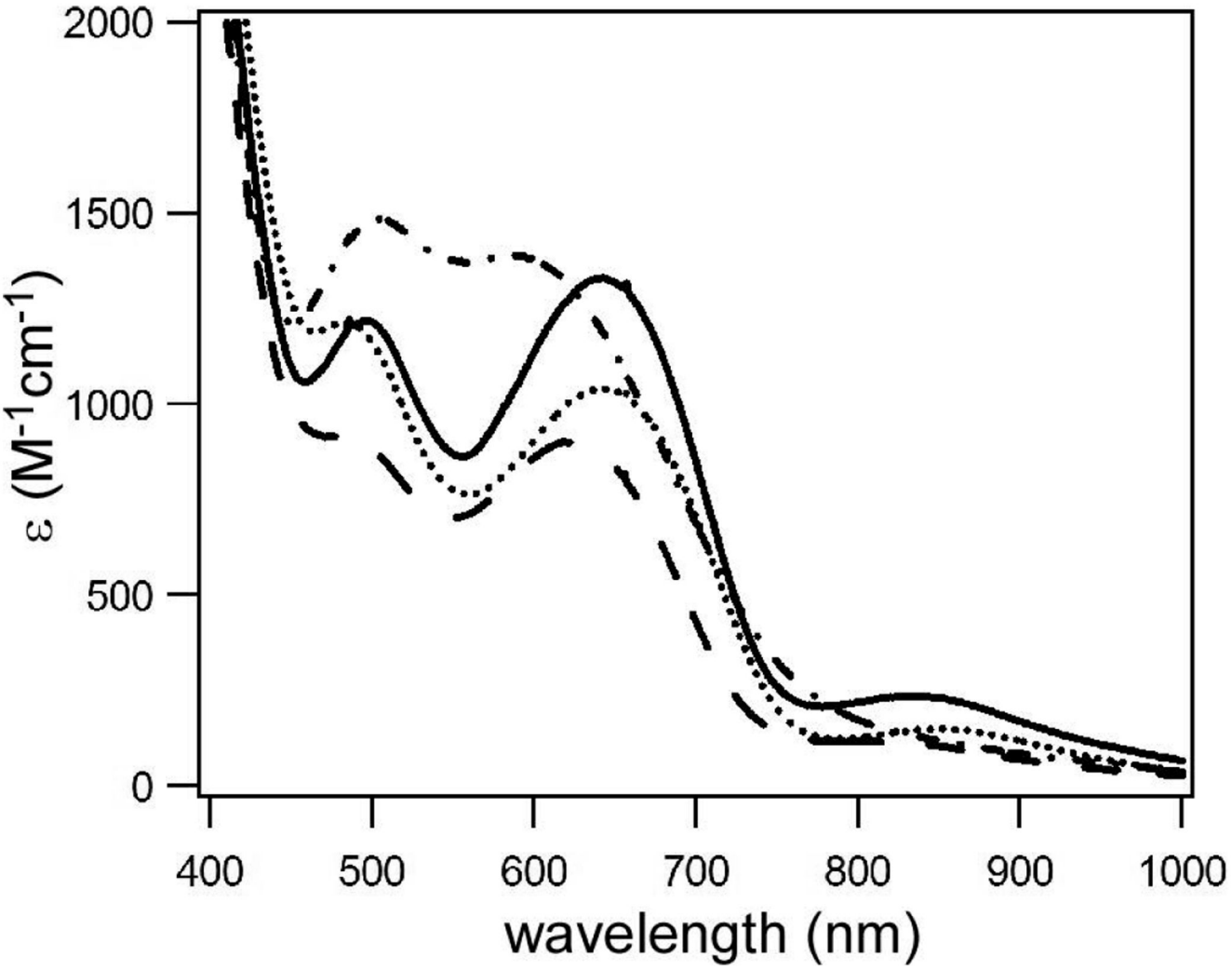

Figure 1.
Visible spectra of $Fe^{III}_2(\mu\text{-}O)(\mu\text{-}1,2\text{-}O_2)$ intermediates, **1** (—), **2** (---), **3** (···), and **4** (-·-) collected in MeCN at −40°C.

NIH-PA Author Manuscript

NIH-PA Author Manuscript

NIH-PA Author Manuscript

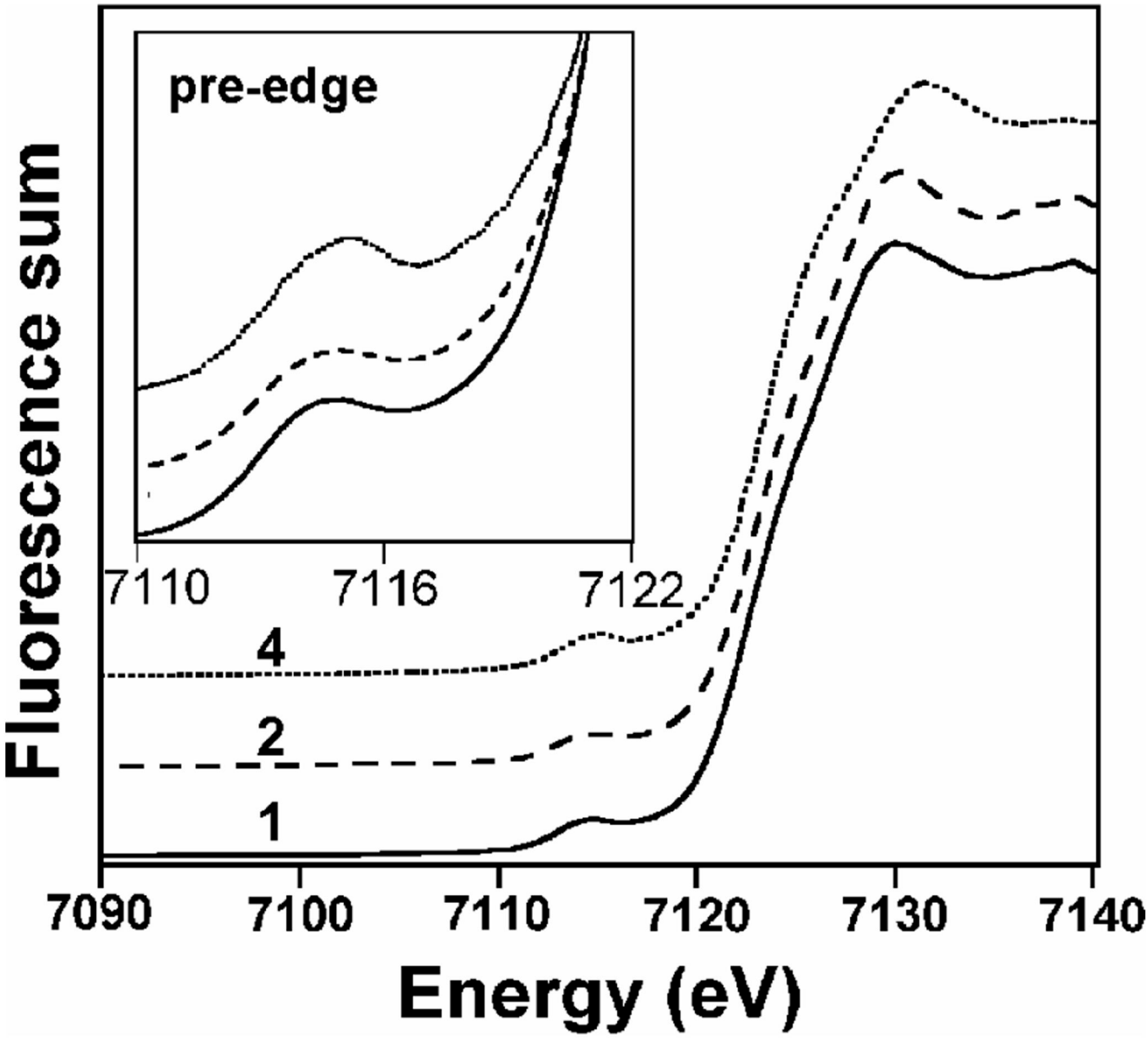

Figure 2.
Fe K-edge X-ray absorption near-edge structures (XANES, fluorescence excitation) of $Fe^{III}_2(\mu\text{-}O)(\mu\text{-}1,2\text{-}O_2)$ intermediates, **1** (—), **2** (---), and **4** (···) measured at ~ 17 K.

NIH-PA Author Manuscript

NIH-PA Author Manuscript

NIH-PA Author Manuscript

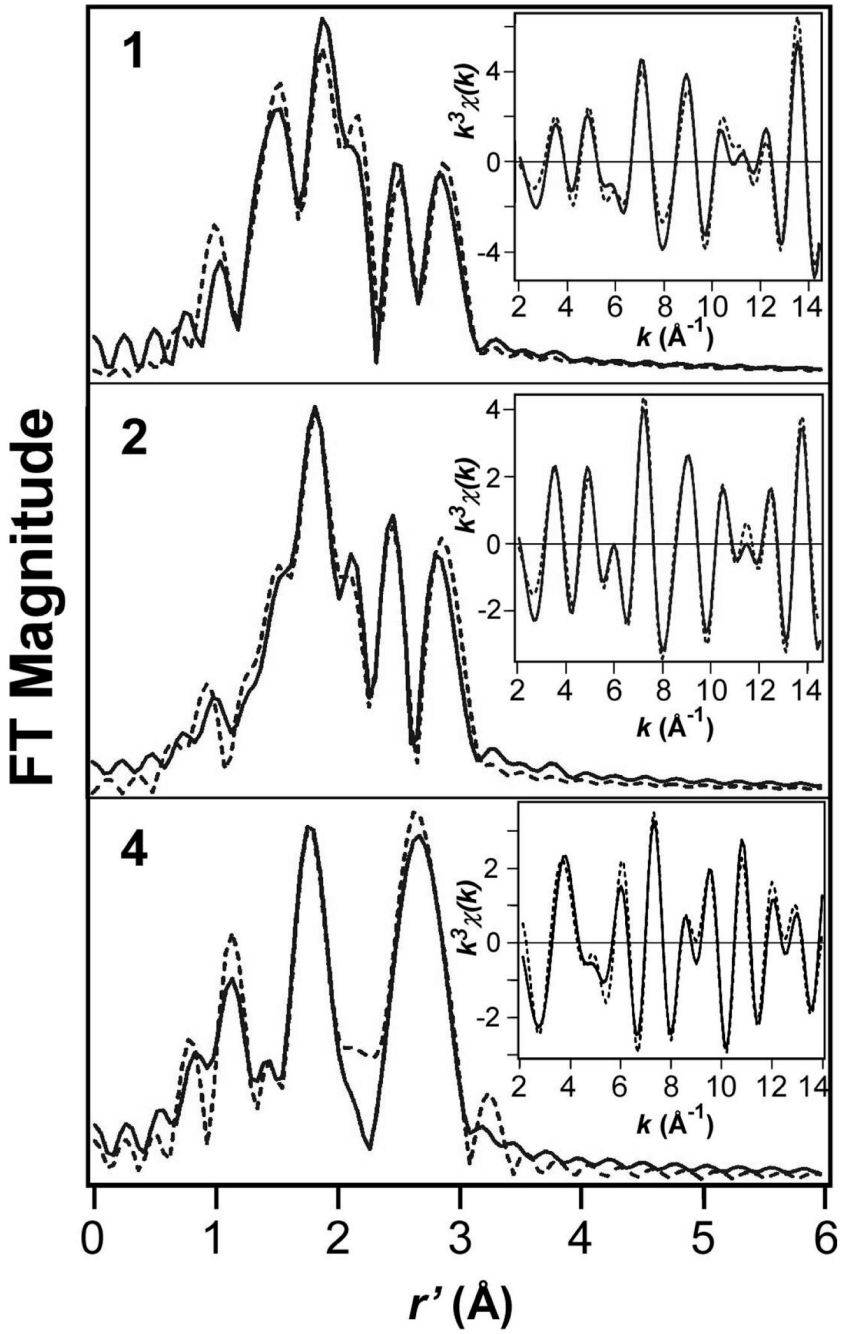

Figure 3.

Fourier transforms of the Fe K-edge EXAFS data ($k^3\chi(k)$) and Fourier-filtered EXAFS spectra ($k^3\chi(k)$, inset) of $[Fe^{III}_2(O)(O_2)(6\text{-MeBQPA})_2]^{2+}$ (**1**, top), $[Fe^{III}_2(O)(O_2)(BQPA)_2]^{2+}$ (**2**, middle) and $[Fe^{III}_2(O)(O_2)(OAc)(BPPE)]^{+}$ (**4**, bottom). Experimental data displayed with dashed (---) lines and fits with solid (—) lines. Back-transformation range: ~0.5 to 3.3 Å; Fourier transformed range: k = 2.0–14.5 Å^{-1} (**1** and **2**) or 2.0–14.0 Å^{-1} (**4**). Fit parameters for each complex are provided in Table 2 in bold and italics.

NIH-PA Author Manuscript

NIH-PA Author Manuscript

NIH-PA Author Manuscript

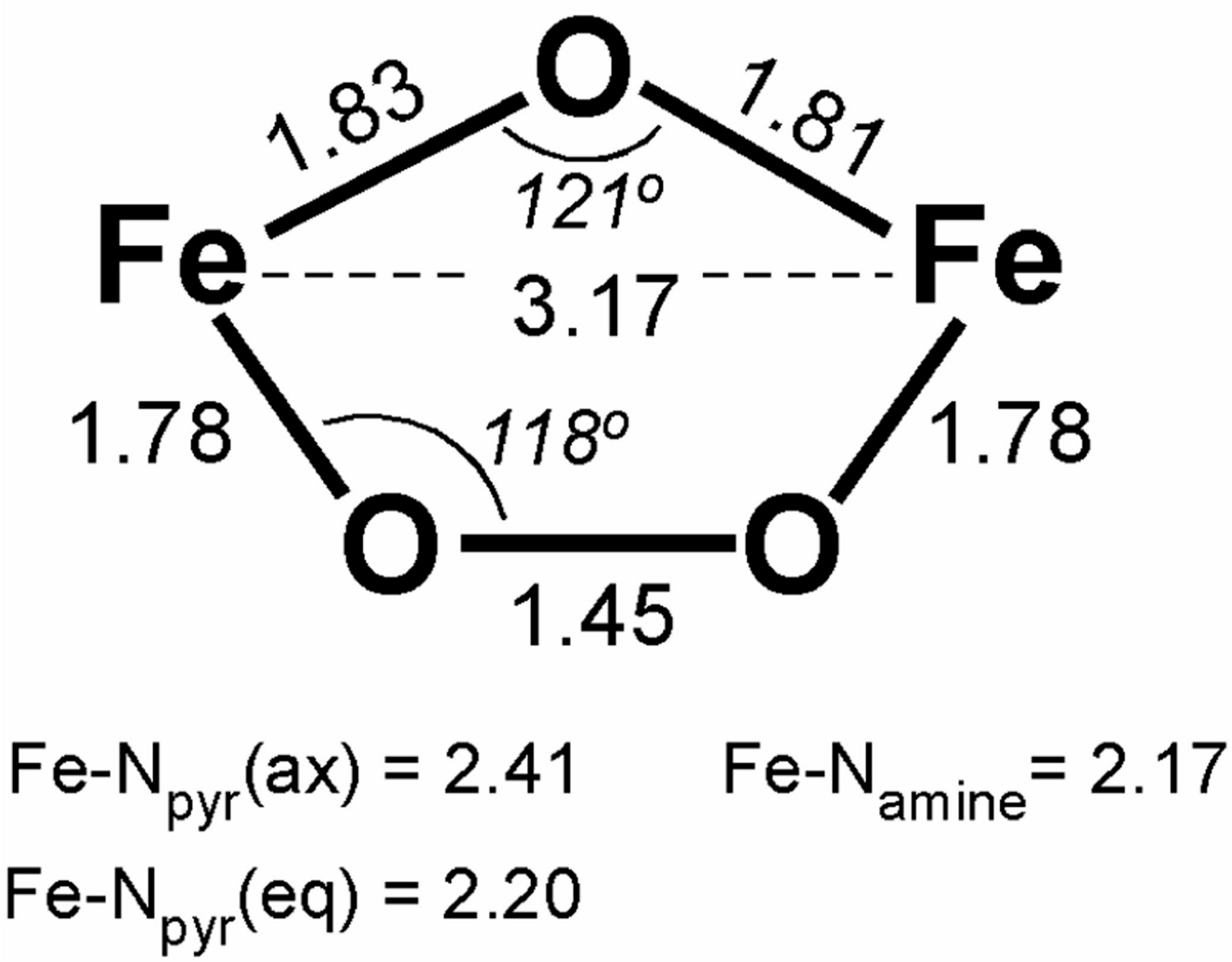

Figure 4.

Schematic showing metrical parameters computed by DFT for $[Fe^{III}_2(O)(O_2)(6\text{-}Me_3\text{-}TPA)_2]^{2+}$ (**3**). All bond distances in Å. The $Fe_2(O)(O_2)$ unit is essentially planar (average dihedral angle = 2.2°). For the Fe-N bond distances, the values have been averaged over the two Fe centers. Differences in coordination geometry between the two sites are minor (< 0.03 Å). See Table S1 for atomic coordinates.

NIH-PA Author Manuscript

NIH-PA Author Manuscript

NIH-PA Author Manuscript

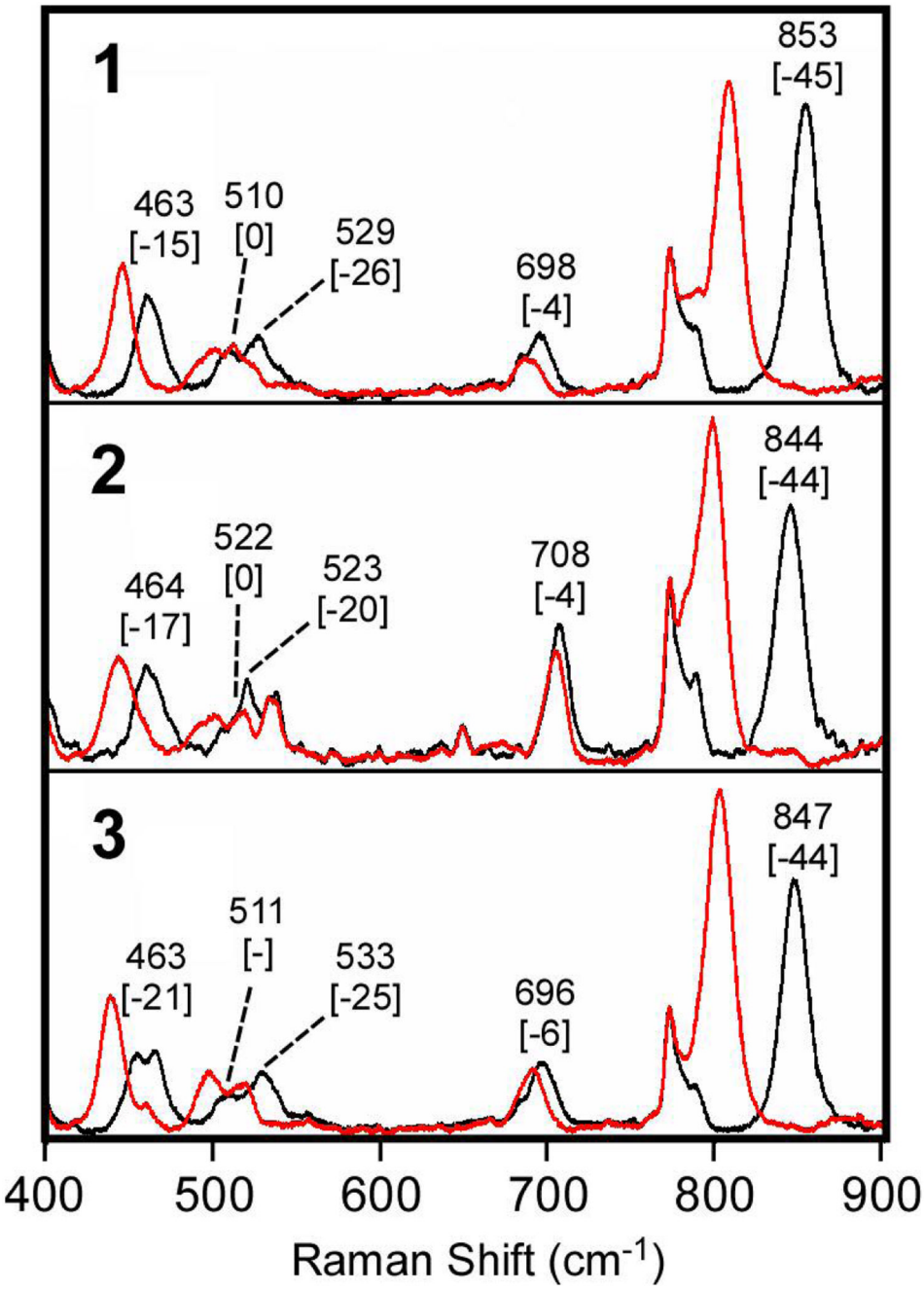

Figure 5.

Resonance Raman spectra obtained with 647.1-nm excitation of frozen CH_3CN solutions of (top) $[Fe_2(\mu\text{-}O)(\mu\text{-}O_2)(6\text{-Me-BQPA})_2]^{2+}$ (**1**) generated with 2 equiv. of Et_3N and 10 equiv. of $H_2{}^{16}O_2$ (black) or $H_2{}^{18}O_2$ (red); (middle) $[Fe_2(\mu\text{-}O)(\mu\text{-}O_2)(BQPA)_2]^{3+}$ (**2**) generated with 2 equiv. of Et_3N and 10 equiv. of $H_2{}^{16}O_2$ (black) or $H_2{}^{18}O_2$ (red); (bottom) $[Fe_2(\mu\text{-}O)(\mu\text{-}O_2)(6\text{-}Me_3\text{-TPA})_2]^{3+}$ (**3**) generated with 2 equiv. of Et3N and 10 equiv. of $H_2{}^{16}O_2$ (black) or $H_2{}^{18}O_2$ (red). Frequencies (in cm^{-1}) are provided for $[Fe_2O_3]$-based modes, with the corresponding $^{16}O_2 \rightarrow {}^{18}O_2$ shifts shown in brackets.

NIH-PA Author Manuscript

NIH-PA Author Manuscript

NIH-PA Author Manuscript

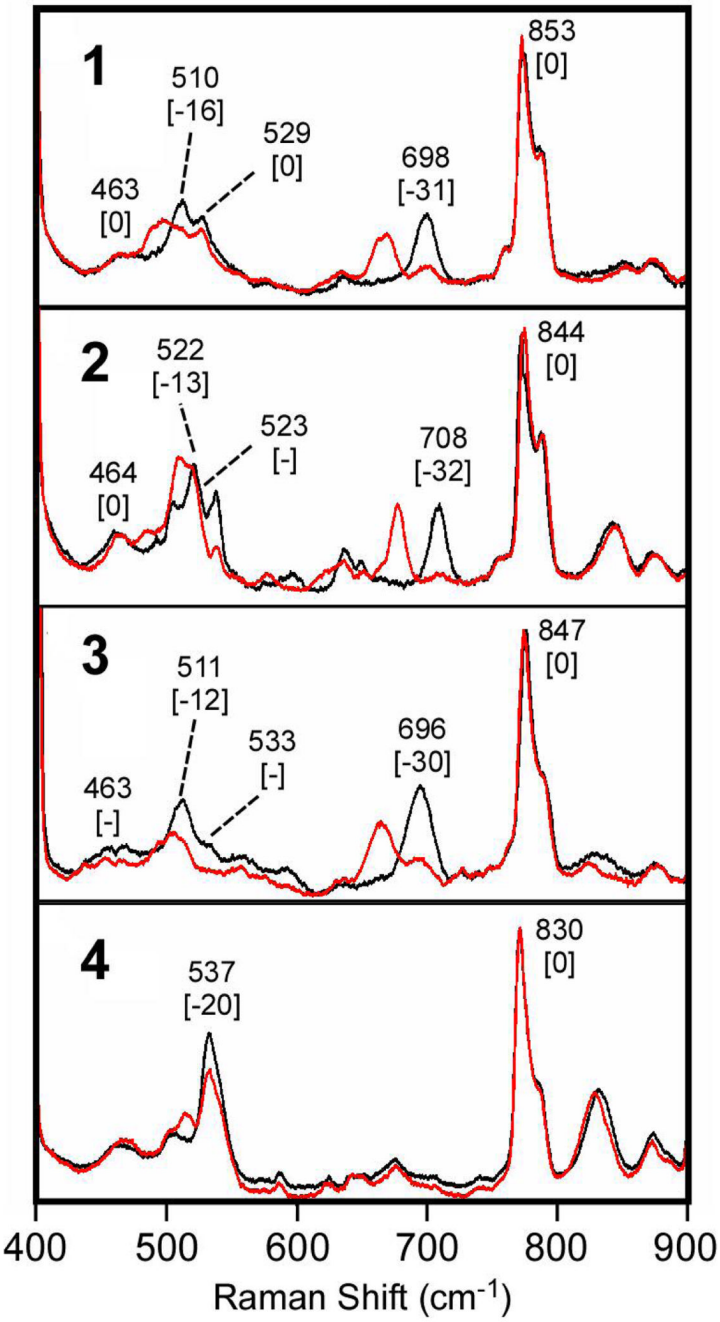

Figure 6.

Resonance Raman spectra of frozen CH_3CN solutions of **1** – **3** obtained with 514.5-nm excitation and for **4** obtained with 457.9-nm excitation. In all cases, the $[Fe_2(\mu\text{-}O)(\mu\text{-}O_2)]$ complexes were prepared with 100 equiv. of $H_2{}^{16}O$ (black) or $H_2{}^{18}O$ (red). Frequencies (in cm^{-1}) are provided for $[Fe_2O_3]$-based modes, with the corresponding $^{16}O \rightarrow {}^{18}O$ shifts shown in brackets.

NIH-PA Author Manuscript

NIH-PA Author Manuscript

NIH-PA Author Manuscript

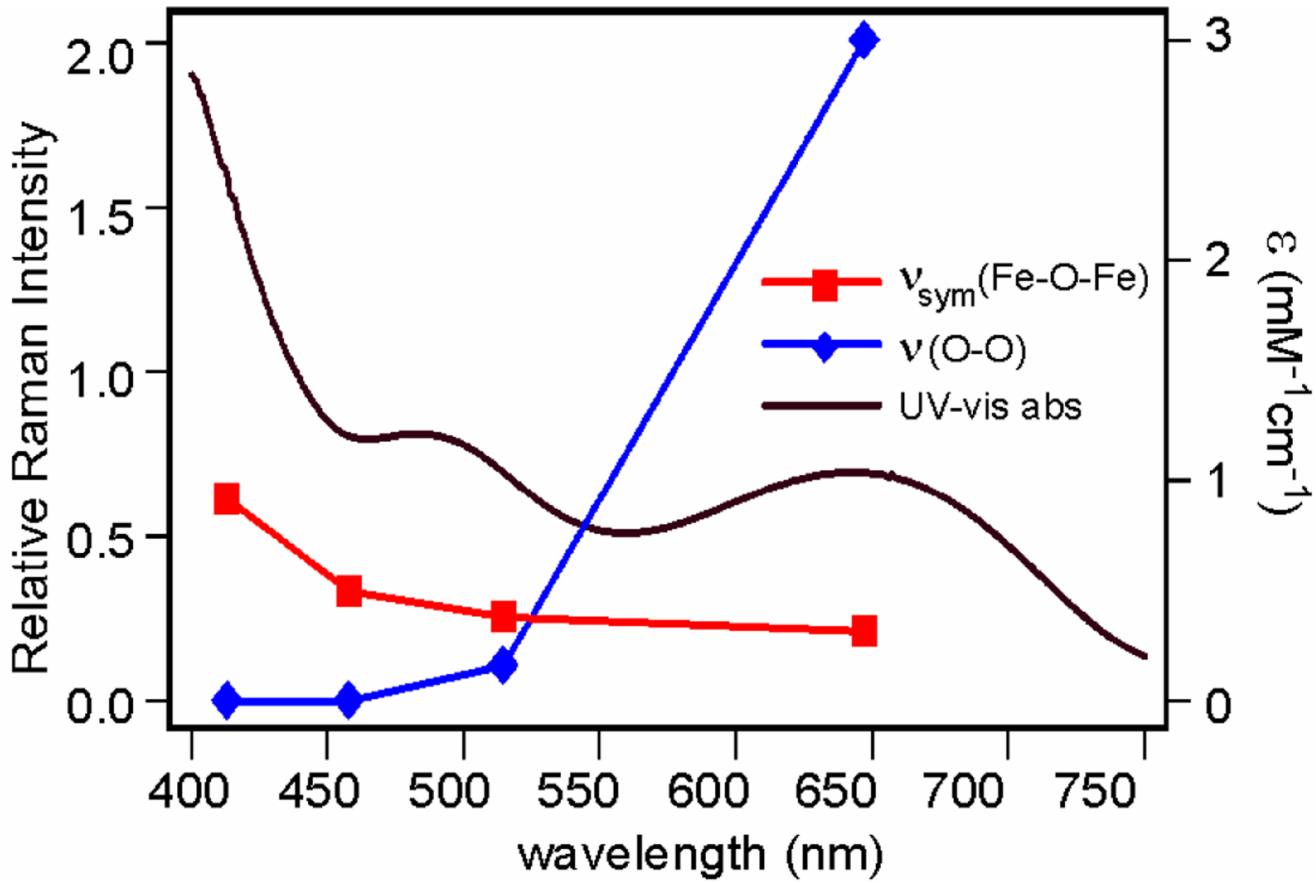

Figure 7.
Resonance Raman excitation profiles of the ν_{sym}(Fe-O-Fe) (–■–) and ν(O-O) (–◆–) vibrations of **3**.

NIH-PA Author Manuscript

NIH-PA Author Manuscript

NIH-PA Author Manuscript

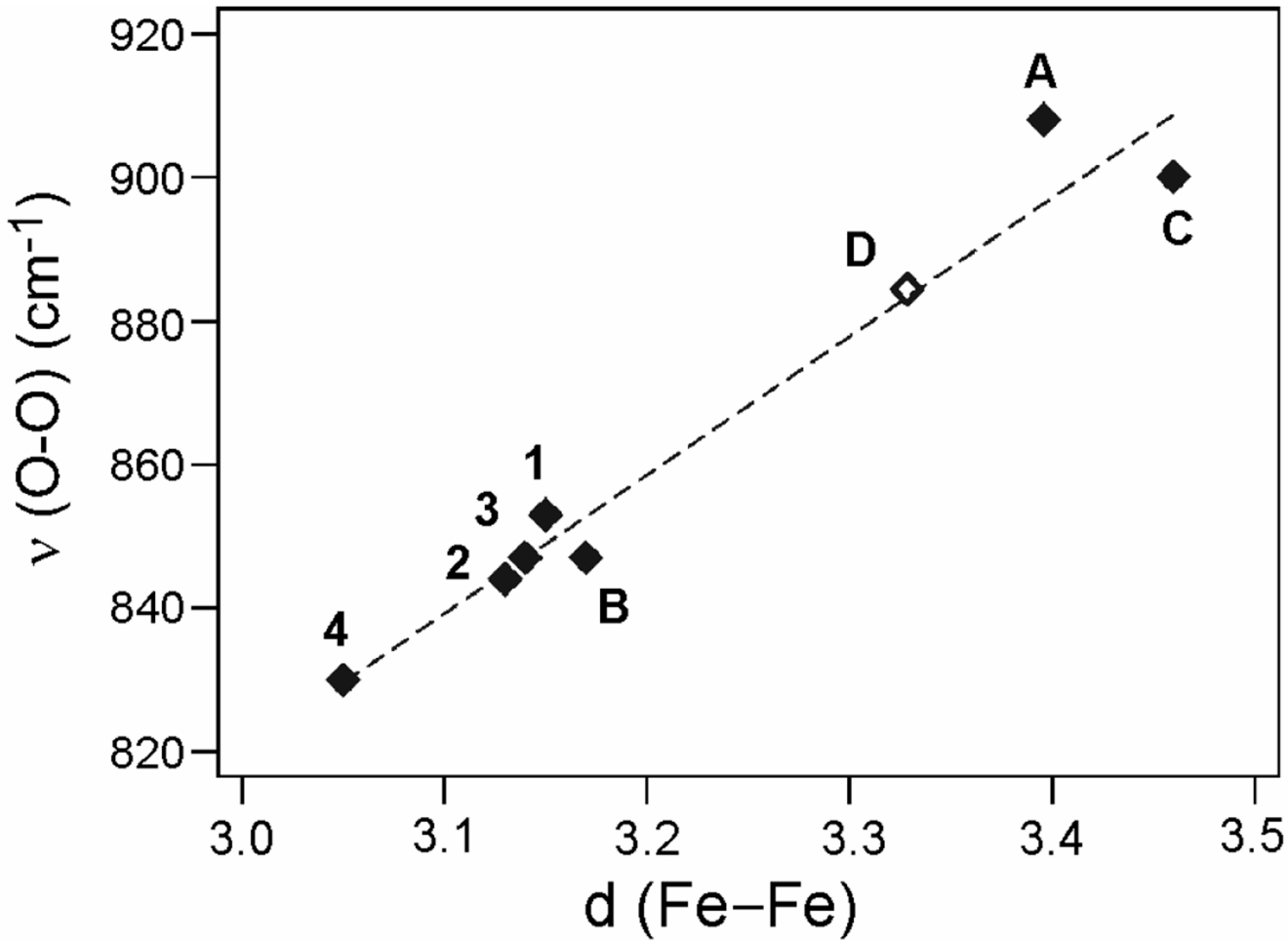

Figure 8.

Plot of O-O stretching frequencies as a function of Fe-Fe distance for **1–4** and related complexes (**A–D**) with $Fe_2(\mu\text{-}1,2\text{-}O_2)(\mu\text{-}OR)$ cores (R = H (**A**), alkyl (**C**), aryl (**D**), or no substituent (**1–4, B**)). Note that since resonance Raman data are not available for **D** (◇), the value used here corresponds to a closely related complex (see Table 3).

NIH-PA Author Manuscript

NIH-PA Author Manuscript

NIH-PA Author Manuscript

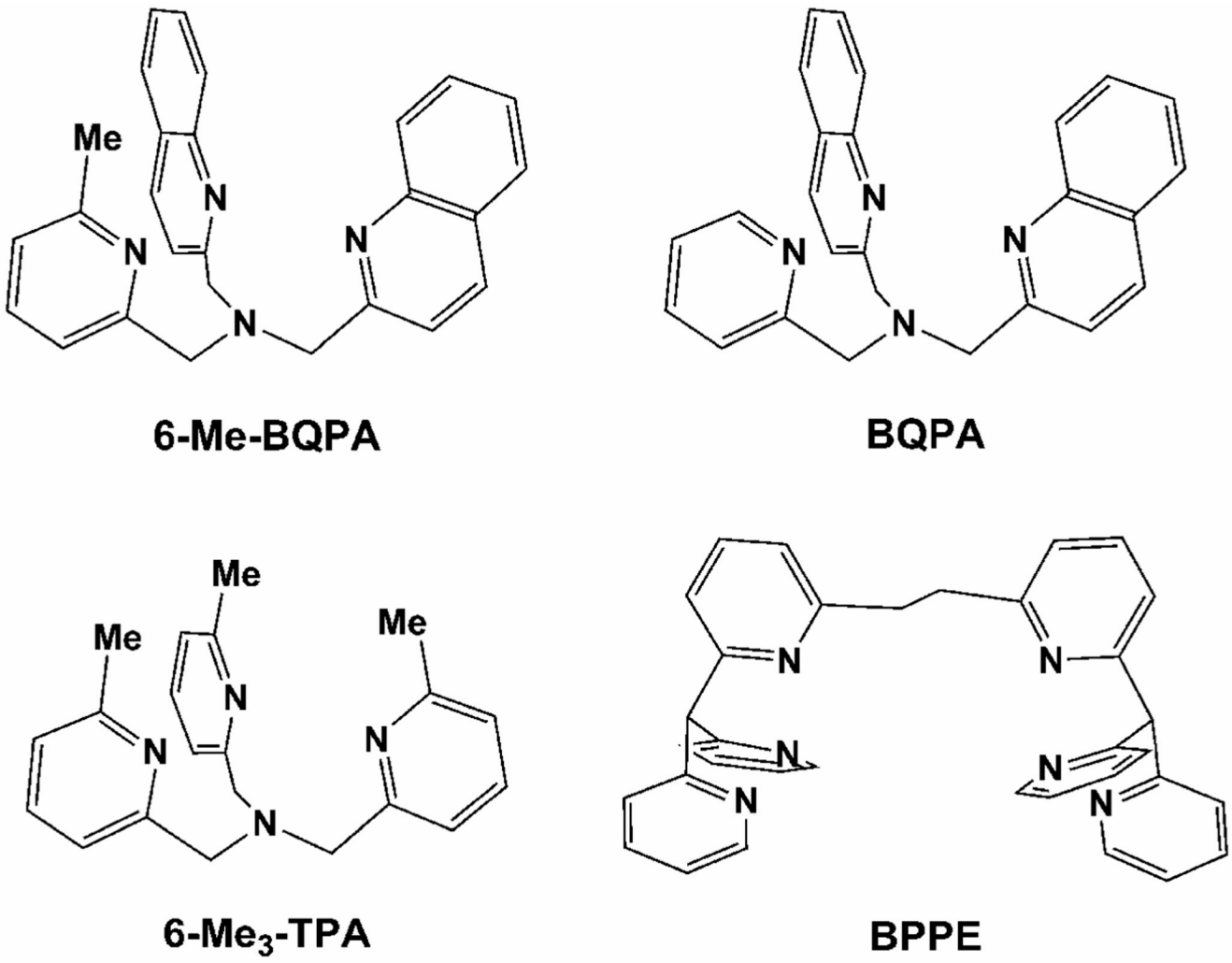

Scheme 1.
Ligands used in this study.

NIH-PA Author Manuscript

NIH-PA Author Manuscript

NIH-PA Author Manuscript

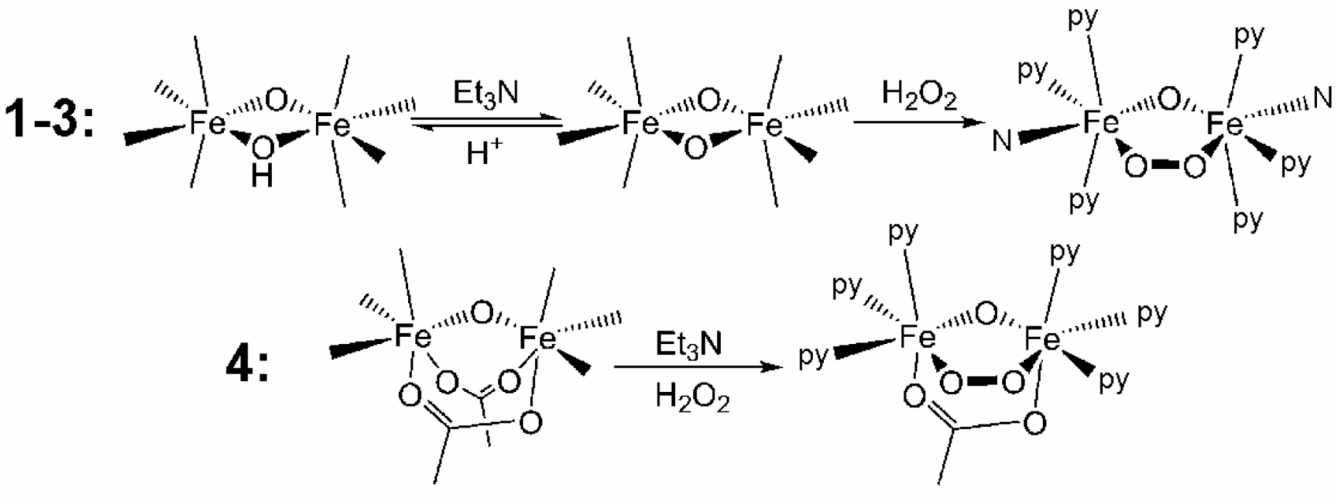

Scheme 2.

Generation of $Fe^{III}_2(\mu\text{-}O)(\mu\text{-}1,2\text{-}O_2)$ complexes of tetradentate ligands 6-Me-BQPA (**1**), BQPA (**2**), and 6-Me_3-TPA (**3**) and hexadentate ligand BPPE (**4**) from respective diiron(III) precursors (see Scheme 1 for ligand structures). The abbreviation "py" represents a pyridine-like ligand, while "N" corresponds to a tertiary amine nitrogen on the polydentate ligand.

NIH-PA Author Manuscript

NIH-PA Author Manuscript

NIH-PA Author Manuscript

Table 1

XAS Near-edge Features and Intensities for Complexes **1**, **2** and **4**.

complex	E_0 (eV)	$E_{pre\text{-}edge}$ (eV)	Pre-edge area
1	7122.8	7114.4	20.4(9)
2	7122.7	7114.5	18.3(9)
4	7123.6	7113.6	29.1(7)

NIH-PA Author Manuscript
NIH-PA Author Manuscript
NIH-PA Author Manuscript

Table 2

EXAFS Fitting Results for $Fe^{III}_2(\mu\text{-}O)(\mu\text{-}1,2\text{-}O_2)$ Intermediates, **1**, **2** and **4**.[a]

		Fe-N/O			Fe-N/O			Fe-N/O			Fe···C			Fe···Fe			GOF[d]
complex	**fit**	**N**	**r(Å)**	**σ^2**	**n**	**r(Å)**	**σ^2**	**n**	**r(Å)**	**σ^2**	**n**	**r(Å)**	**σ^2**	**n**	**r(Å)**	**σ^2**	
1	1							6	2.23	4.5							416
	2	2	1.83	4.7				4	2.24	1.8							253
	3	2	1.84	6.7				4	2.25	2.4				1	3.19	3.4	246
	4	2	1.83	5.4				4	2.25	1.4	6	3.00	2.0	1	3.16	1.5	125
	5	2	1.83	4.7				3	2.24	0.9	6	3.01	2.7	1	3.16	1.8	94
	6	2	1.83	5.0				3	2.24	1.0	4	3.00	0.3	1	3.15	2.2	90
	7	***2***	***1.83***	***3.7***	***1***	***2.05***	***1.0***[b]	***3***	***2.23***	***0.3***	***4***	***2.99***	***1.1***	***1***	***3.15***	***3.0***	***43***
2	1							6	2.22	6.5							270
	2	2	1.85	12.0				4	2.22	3.8							173
	2	2	1.85	11.5				4	2.23					1	3.14	5.0	123
	3	2	1.84	11.1				4	2.21	4.3	6	2.99	2.1	1	3.14	1.3	35
	4	2	1.85	11.6				4	2.21	4.4	4	2.98	0.1	1	3.12	1.6	30
	5	2	1.84	12.4				3	2.21	2.8	4	2.98	0.3	1	3.12	1.8	27
	6	2	1.81	5.0[b]	1	2.02	1.2	3	2.20	1.8	4	2.97	0.9	1	3.12	2.6	26
	7	2	1.81	5.0[b]	1	2.02	1.1	3	2.20	1.7	6	2.98	2.8	1	3.13	2.1	23
	8	***2***	***1.82***	***6.7***	***1***	***2.03***	***3.4***	***3***	***2.21***	***1.7***	***6***	***2.98***	***2.6***	***1***	***3.13***	***1.9***	***16***
4	1							6	2.18	10.0[b]							300
	2	2	1.88	10.4				4	2.16	6.9							164
	3	2	1.88	10.5				4	2.16	6.4				1	3.06	2.20	28
	4	2	1.87	10.1				4	2.16	6.7	6	3.08	2.1				34
	5	2	1.88	10.5				4	2.17	6.5	4	3.15	13.3	1	3.06	2.69	21
	6	1	1.86	4.7				5	2.16	11.2				1	3.06	2.64	44
	7	1	1.88	5.11				4	2.16	7.8				1	3.06	2.60	34
	8	1	1.78	3.39	1	1.92	0.4	4	2.14	6.2				1	3.05	2.44	18
	9	***1***	***1.77***	***5.83***	***2***	***1.94***	***6.5***	***3***	***2.16***	***3.2***				***1***	***3.04***	***2.32***	***19***

NIH-PA Author Manuscript
NIH-PA Author Manuscript
NIH-PA Author Manuscript

		Fe-N/O			Fe-N/O			Fe-N/O			Fe···C			Fe···Fe			GOF[d]
complex	**fit**	**N**	**r(Å)**	**σ^2**	**n**	**r(Å)**	**σ^2**	**n**	**r(Å)**	**σ^2**	**n**	**r(Å)**	**σ^2**	**n**	**r(Å)**	**σ^2**	
	10	2	1.88	11.98	1	1.98	4.3	3	2.16	3.2				1	3.05	2.34	20
3[c]		2	1.84					4	2.23		6	2.96		1	3.14		

[a]Back-transformation range: ~ 0.50 to 3.3 Å; Fourier-transformed range: k = 2.0 – 14.5 $Å^{-1}$ (**1** and **2**), 2.0 – 14.0 $Å^{-1}$ (**4**). Resolution = ~ 0.12 Å. σ^2 in units of $Å^2$. The first two shells were fit using a scatter with oxygen parameters, whereas the third employed nitrogen parameters; however, backscatters differing by Z = 1 cannot be distinguished by EXAFS.

[b]σ^2-value held fixed during optimization.

[c]Reference 15

[d]GOF = goodness of fit.

NIH-PA Author Manuscript NIH-PA Author Manuscript NIH-PA Author Manuscript

Table 3

Raman vibrational frequencies (cm^{-1}) for $Fe^{III}_2(\mu\text{-}O)(\mu\text{-}1,2\text{-}O_2)$ intermediates **1–4** and Related Complexes **A–E**.

Complex	ν_{sym} (Fe-O-Fe) [$\Delta^{18}O$, $\Delta^{18}O_2$]	ν_{asym} (Fe-O-Fe) [$\Delta^{18}O$, $\Delta^{18}O_2$]	ν(O-O) [$\Delta^{18}O$, $\Delta^{18}O_2$]	ν_{sym} (Fe-O_2-Fe) [$\Delta^{18}O$, $\Delta^{18}O_2$]	ν_{asym} (Fe-O_2-Fe) [$\Delta^{18}O$, $\Delta^{18}O_2$]	d (Fe-Fe)
1	510 [−16, 0]	698 [−31, −4][a]	853 [0, −45]	463 [0, −15]	529 [0, −26]	3.15 Å
2	522 [−13, −]	708 [−32, −4]	844 [0, −44]	464 [0, −17]	523 [−, −20]	3.13 Å
3	511 [−12, −]	696 [−30, −6]	847 [0, −44]	463 [−, −21]	533 [−, −25]	3.14 Å
4 [b]	537 [−20, −]	– [−, −]	830 [0, −]	– [−, −]	– [−, −]	3.04 Å
A [c]			908 [−, −47]	460 [−, −13]	548 [−, 12]	3.40 Å
B [d]	-	695 [−, −2]	847 [−, −33]	465 [−, −19]	-	3.17 Å
C [e]			900 [−, −50]	471 [−, −16]		3.46 Å
D [f]			(884) [g]			3.33 Å
E [h]			876 [−, −48]	421 [−, −12]		4.00 Å

[a] Downshift of −35 cm^{-1} observed for the fully labeled $Fe_2(^{18}O)(^{18}O_2)$ core.

[b] Although the resonance Raman spectrum of **4** was previously published in ref [17], the reported frequency of the ν(O-O) mode (816 cm^{-1}) differs from the value of 830 cm^{-1} listed here, which was obtained in our laboratory for direct comparisons with data for the other peroxo complexes we investigated.

[c] **A** = $[Fe_2(\mu\text{-}OH)(\mu\text{-}1,2\text{-}O_2)(6\text{-}Me_2BPP)]^+$ (6-Me_2BPP = *N*,*N*-bis(6-methyl-2-pyridylmethyl)-3-aminopropionate).[14]

[d] **B** = $[Fe_2(\mu\text{-}O)(\mu\text{-}1,2\text{-}O_2)(6\text{-}Me_2BPP)]$.[14]

[e] **C** = $[Fe_2(\mu\text{-}1,2\text{-}O_2)(N\text{-Et-HPTB})(OPPh_3)_2]^{3+}$ (*N*-Et-HPTB = anion of *N*,*N*,-*N*',*N*'-tetrakis(1'-ethylbenzimidazolyl-2'-methyl)-2-hydroxy-1,3-diaminopropane). [12,42] The Raman vibrational frequencies were obtained in our laboratory (see Figure S2 in the Supporting Information).

[f] **D** = $[Fe_2(\mu\text{-}1,2\text{-}O_2)(PhCOO)(Ph\text{-bimp})]^{2+}$ (Ph-bimp = 2,6-bis[bis[2-(1-methyl-4,5-diphenylimidazolyl)methyl)aminomethyl]-4-methylphenolate [11]

NIH-PA Author Manuscript
NIH-PA Author Manuscript
NIH-PA Author Manuscript

[g] Frequency was obtained for the related complex $[Fe_2(\mu\text{-}1,2\text{-}O_2)(CH_3COO)(L)]^{2+}$ (L = *N,N'*-(2-hydroxy-5-methylxylylene) bis(*N*-carboxymethylglycine)).[43]

[h] **E** = $[Fe_2(\mu\text{-}1,2\text{-}O_2)(PhCH_2CO_2)_2(Tp^{iPr2})_2]^{2+}$ (Tp^{iPr2} = HB(pz')$_3$, where pz' is 3,5-bis(isopropyl)-pyrazolyl.)[13,44]

NIH-PA Author Manuscript NIH-PA Author Manuscript NIH-PA Author Manuscript

Table 4

Comparison of Experimental and NCA-Calculated Vibrational Data for **1**.

mode		frequency	isotope shifts		
			$\Delta^{18}O$	$\Delta^{18}O_2$	$\Delta(^{18}O, {}^{18}O_2)$
ν_{sym}	exp	510	−16	0	−18
(Fe-O-Fe)	NCA	513	−18	−1	−20
ν_{asym}	exp	698	−31	−4	−35
(Fe-O-Fe)	NCA	697	−31	−2	−33
ν(O-O)	exp	853	0	−45	−47
	NCA	854	0	−48	−49
ν_{sym}	exp	463	0	−16	−19
(Fe-O_2-Fe)	NCA	461	−1	−19	−20
ν_{asym}	exp	529	0	−26	−22
(Fe-O_2-Fe)	NCA	531	−2	−22	−23

NIH-PA Author Manuscript

NIH-PA Author Manuscript

NIH-PA Author Manuscript

Table 5

Force Constants Obtained from Normal Coordinate Analyses for **1** and **B.**

	Force constants (mdyn/Å)	
Internal coordinate	**L = 6-MeBQPA (1)**	**L = 6-Me_2BPP (B)** [a]
r (Fe-O_{oxo})	2.86	2.54
r (Fe-O_{peroxo})	2.17	1.84
r (O-O)	3.17	3.25

[a] Reference 14